Alexandria Engineering Journal (2020) 59, 191–207

HOSTED BY
ELSEVIER

Alexandria University

Alexandria Engineering Journal

www.elsevier.com/locate/aej
www.sciencedirect.com

ORIGINAL ARTICLE

Numerical study of melting-process of a non-Newtonian fluid inside a metal foam

S.A.M. Mehryan [a], Mohammad H. Heidarshenas [b], Ahmad Hajjar [c], Mohammad Ghalambaz [d,e,*]

[a] Young Researchers and Elite Club, Yasooj Branch, Islamic Azad University, Yasooj, Iran
[b] Department of Mechanical Engineering, Shahid Chamran University of Ahvaz, Ahvaz, Iran
[c] LabECAM, ECAM Lyon, Université de Lyon, Lyon, France
[d] Department for Management of Science and Technology Development, Ton Duc Thang University, Ho Chi Minh City, Viet Nam
[e] Faculty of Applied Sciences, Ton Duc Thang University, Ho Chi Minh City, Viet Nam

Received 26 August 2019; revised 1 December 2019; accepted 7 December 2019
Available online 19 December 2019

KEYWORDS

Phase Change Material (PCM);
Non-Newtonian PCM;
Porous medium;
Arbitrary Eulerian-Lagrangian (ALE);
Stefan condition

Abstract Non-Newtonian behavior of a Phase Change Material (PCM) inside a porous coaxial pipe is studied by utilizing the deformed mesh technique. The inner and outer pipes are subjected to the high and low temperatures of T_h and T_c, while the bottom and upper surfaces are thermally insulated. The Finite Element Method (FEM), implemented in the Arbitrary Eulerian-Lagrangian (ALE) moving grid technique, is applied to solve the weakened forms of the governing equations. Stefan's condition is employed to track the solid-liquid interface of the PCM during the melting process. Grid independency test is conducted, and the verifications of the results are evaluated through comparisons with several test cases published in the literature. The simulations show that an increment of Stefan's number can significantly improve the melting rate. As the Stefan number reaches from 0.014 to 0.01, the full melting non-dimensional time declines from 1.313 to 0.937. Also, an extreme increase in the melting rate can be found while decreasing the power-law index. When the power-law index decrease from 1 to 0.6, the full melting time subsequently is reduced to 54%.

1. Introduction

The excessive needs in energy in recent years have increased the efforts aiming to a better investment of renewable energy resources and more efficient energy storage techniques. In this context, Thermal Energy Storage (TES) has drawn much attention in the past few decades. More particularly, latent heat storage using Phase Change Materials (PCM), an essential technique of TES, has been an active research area in

* Corresponding author at: Ton Duc Thang University, Ho Chi Minh City, Vietnam.
E-mail address: mohammad.ghalambaz@tdtu.edu.vn (M. Ghalambaz).
Peer review under responsibility of Faculty of Engineering, Alexandria University.

https://doi.org/10.1016/j.aej.2019.12.021

Nomenclature

C_p	heat capacity at constant pressure	β	thermal expansion coefficient
I	unit matrix	μ	dynamic viscosity
$\vec{g}$	gravity acceleration	ϕ	volume fraction
L_{fs}	latent heat	ϕ_{wt}	mass fraction
m	consistency of dynamic viscosity		
n	power-law index of the non-Newtonian fluid	*Subscripts*	
p	dimensional pressure	c	cold
P	non-dimensional pressure	f	fluid
s	solid PCM	fu	fusion temperature
t	dimensional time	h	hot
T	temperature	nf	nano-PCM at fluid phase
tr	transpose of the matrix	np	nanoparticles
		ns	nano-PCM at the solid phase
Greek symbols		wt	weight quantity
ρ	density		

recent years [1,2]. This is due to the fact that PCM can store a large amount of energy for a small volume change and a small temperature difference. Thermal storage and release occur during the phase change of PCM, either by melting or by solidification. However, the main drawback of PCM is their low thermal conductivity, which slows down the heat transfer and reduces system efficiency. Thus, several heat-transfer enhancement techniques have been tested, such as PCM encapsulation [3–6], the use of nano additives [7–10], non-metallic foams [11], finned tubes [12], metallic matrix structures [13], and metallic fins [14–16]. A summary of the various enhancement techniques can be found in the comprehensive reviews of [2,17].

The metal foams have also been used as a thermal conductivity enhancement for PCM, as these foams present a low density for a large surface area. Siahpush et al. [18] found, both experimentally and analytically, that using copper foam increased up to seven times the thermal conductivity of PCM during melting and solidification. Zhao et al. [19] performed an experimental study and concluded that the material of the foam, as well as its structure, play an essential role in the thermal conductivity enhancement. Xiao et al. [20,21] used vacuum impregnation to prepare composite structures of paraffin as PCM and Nickel and Copper as the metal foam. They found that the effective thermal conductivity of the composite structure is substantially higher than that of pure paraffin. Lafdi et al. [22] in their experiments focused on aluminum foam on the impact of porosity and pore size on heat transfer. Their results showed that increasing the foam porosity changed the heat transfer from being conduction dominated to convection dominated and consequently shortened the time needed to reach the steady-state temperature.

The effect of metallic foam on heat transfer enhancement has been also investigated numerically. For instance, Chen et al. [23] performed a numerical study using the Lattice Boltzmann method to compare a PCM-metal composite structure to pure PCM. They observed that the composite structure presented a higher melting rate, and the presence of the metal inhibited the effect of natural convection. Similarly, Tian and Zhao [24] found in their numerical investigation that the heat transfer of a PCM-metal structure can be seven times higher than a pure PCM system. Jourabian et al. [25,26] aimed to study numerically the effect of porosity on the phase change of ice and other PCM in annular cavities. Their results, following the experimental studies mentioned previously [22], indicated that lowering the porosity lead to higher effective conductivity and decreased the effect of convection. In a recent numerical study, Dinesh and Bhattacharya [27] concluded that the geometrical parameters of the metallic foam, such as porosity, pore size, and pore overlap should be selected based on the required energy absorption duration, as a shorter duration can be achieved by decreasing the overall porosity and the pore overlap.

When dealing with the natural convection flow of PCM in a cavity, the flow rheological behavior should be taken into consideration. It has been shown that some PCM exhibit non-Newtonian behavior [28]. Natural convection has been widely investigated for Newtonian fluids in enclosures [29], in cavities with single or multiple layers of porous media [30,31], cavities with wavy walls [32], cavities filled with porous fins [33] and in tilted cavities [34]. Moreover, several works gave attention to the natural convection of nanofluids in porous cavities [35,36]. The problem of free convection of non-Newtonian fluids has also been addressed. Different channel cavities have been considered, such as square [37] and L-shaped [38] cavities, the space between two plates [39,40] or between eccentric annulus [41], as well as in trapezoidal cavities filled with a porous medium [42]. Other works investigated the natural convection of non-Newtonian nanofluids in porous enclosures [43,44].

Nonetheless, studies dealing with the natural convection of PCM with non-Newtonian behavior in porous cavities is a new subject. The present paper attempts to fill this gap by considering the melting of a non-Newtonian phase change materials, modeled as a power-law fluid, embedded in an aluminum foam contained between two co-axial pipes with different temperatures for the first time.

2. Modeling

2.1. Physics of the problem

Two coaxial pipes having the height of L, as depicted in Fig. 1, are studied. The inner pipe of radius r_i is held at a high-temperature T_h, while the outer pipe of radius r_o is cold with a low-temperature T_c. The remaining two bounds are perfectly insulated using an insulating substance. Aluminum foam, between inner and outer pipes, is modeled as a homogenous porous medium (Table 1). Viscous dissipation effect on the temperature field and, consequently, on the velocity through buoyancy, is ignorable. Depicted in Fig. 1, the problem is axisymmetric with respect to θ direction. The problem, therefore, can be studied as a 2D one in (r, z) coordinates. Firstly, the substance filling the pores is solid with the same uniform temperature throughout the porous medium. The molten substance behaves as a power-law non-Newtonian fluid (Table 2). It is assumed that the density variations during heating and melting processes are not dramatic. Hence, the Boussinesq approximation can be utilized to estimate the buoyancy force.

2.2. Governing equations

Considering the assumptions, explained in the physical model, the governing equations describing the thermal and hydrodynamic behavior of the molten substance flow can be expressed as [4]:

$$\rho_f \nabla^* \cdot \vec{u} = 0 \tag{1}$$

$\vec{u}$ in the above-written equation is the velocity vector including u_r and u_z components along with the r and z directions, respectively. ρ_f is the fluid density. Besides, ∇^* is the gradient vector in the r-z dimensional space [43,45].

$$\frac{\rho_f}{\varepsilon}\frac{\partial \vec{u}}{\partial t} + \frac{\rho_f}{\varepsilon^2}\cdot(\vec{u}\cdot\nabla^*)\vec{u} = \nabla^*\cdot\left[-pI + \frac{\mu}{\varepsilon}\left(\nabla^*\vec{u} + (\nabla^*\vec{u})^{tr}\right)\right] - \frac{\mu}{\kappa}\vec{u} + \rho_f\vec{g}\beta\Delta T \tag{2}$$

in which t is the time, ε is the porosity, p is the pressure, μ is the dynamic viscosity, β is the thermal expansion coefficient, κ is the permeability and $\vec{g}$ is the gravity vector, and I is the unit matrix. The superscript tr denotes the transpose of the matrix. The power-law model describes the molten substance flow. The variations of dynamic viscosity according to the shear rate is expressed below [43]:

$$\mu(\dot{\gamma}) = m\mu_a \ \exists \begin{cases} \mu_a = (\dot{\gamma})^{n-1} \\ \dot{\gamma} = max\left(\sqrt{[D'] : [D']},\ \dot{\gamma}_{min}\right) \\ 2D' = \left(\nabla\vec{u} + (\nabla\vec{u})^{tr}\right) \end{cases} \tag{3}$$

in which m and n are respectively the consistency of dynamic viscosity and power-law index of the non-Newtonian fluid. The non-Newtonian fluids are respectively called pseudoplastic and dilatant for $n < 1$ and $n > 1$. Evidently, the fluid is Newtonian for $n = 1$. These classifications are based on the variations of an apparent viscosity as shear stress increases. For the pseudoplastic fluids, the apparent viscosity declines with an increase of shear rate; however, the apparent viscosity of the dilatant fluids augments with an increment of shear rate.

Table 1 Thermo-physical properties of the solid matrix.

Property[Unit]	Symbol	Value
Density [kg/m^3]	ρ_p	2700
Porosity	ε	0.9
Thermal conductivity [W/m K]	k_p	200
Specific heat [J/kg K]	$C_{p,p}$	897

Table 2 Thermophysical properties of the paraffin wax.

Property[Unit]	Symbol	Value
Thermal expansion coefficient [1/K]	β	6×10^{-4}
Density (solid/liquid) [kg/m^3]	ρ_s/ρ_l	880/760
Melting temperature [K]	T_{fu}	318–324
Thermal conductivity [W/m K]	k	0.2
Latent heat of fusion [kJ/kg]	L_{fs}	168
Specific heat [J/kg K]	C_p	2000
Dynamic viscosity [kg/m s]	μ	6×10^{-3}

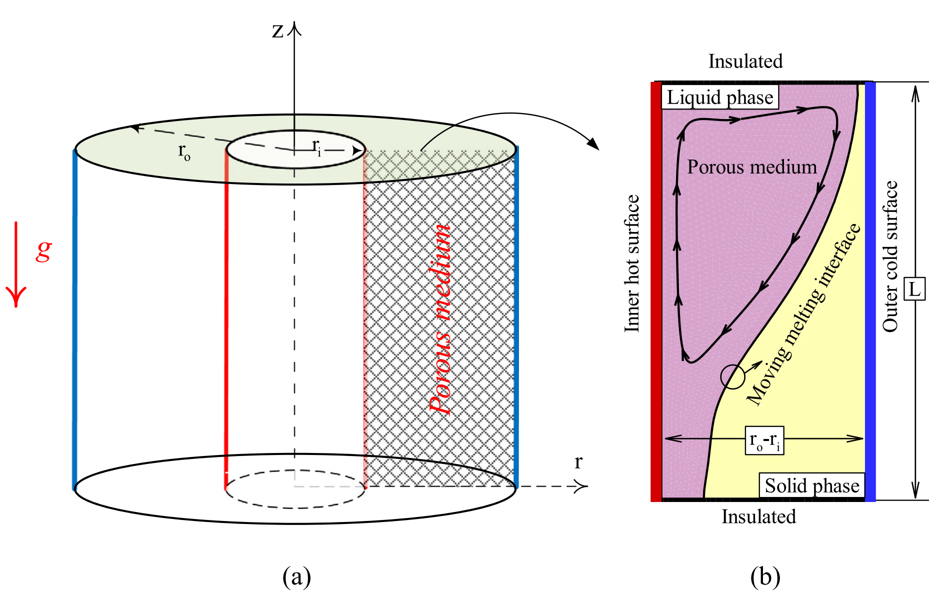

Fig. 1 Schematic representation of the problem physics (a) 3D and (b) 2D.

Table 3 The grid size and required time for grid-check.

Case number	Liquid mesh size		Solid mesh size		number of grid points at the melting interface	$Fo = 0.1$		$Fo = 1.5$	
	Max	Min	Max	Min		MVF	*Error (%)	MVF	Error(%)
1	0.015	0.01	0.07	3e−4	100	0.48647	0.214	0.92935	0.365
2	0.0125	0.01	0.05	3e−4	140	0.48535	0.016	0.93045	0.248
3	0.011	0.007	0.06	3e−4	130	0.48543	–	0.93276	–

$* Error = \left|\frac{MVF_{case3} - MVF}{MVF_{case3}}\right| \times 100.$

Energy balance equation for the sub-domain of the molten substance is expressed as follows [46]:

$$(\rho C_p)_{eff,f}\frac{\partial T}{\partial t} + (\rho C_p)_f\vec{u}\cdot\nabla^* T = \nabla^*\cdot(k_{eff,f}\nabla^* T) \quad (4)$$

In which

$$(\rho C_p)_{eff,f} = \varepsilon(\rho C_p)_f + (1-\varepsilon)(\rho C_p)_p \quad (5a)$$

$$k_{eff,f} = \varepsilon k_f + (1-\varepsilon)k_p \quad (5b)$$

Eventually, the energy equation for the solid portion of the PCM is written as follows [46]:

$$(\rho C_p)_{eff,s}\frac{\partial T}{\partial t} = \nabla\cdot(k_{eff,s}\nabla T) \quad (6)$$

where

$$(\rho C_p)_{eff,s} = \varepsilon(\rho C_p)_s + (1-\varepsilon)(\rho C_p)_p \quad (7a)$$

$$k_{eff,s} = \varepsilon k_s + (1-\varepsilon)k_p \quad (7b)$$

In the equations mentioned above, T is the temperature, and C_p is the heat capacity at constant pressure. The s and f subscripts denote the fluid and solid PCMs. The volumetric changes of the substance during the melting is considered to be ignorable. Hence, the density of solid and liquid phase change substance is the same, (i.e. $\rho_f = \rho_s$):

The energy balance on the forwarding interface boundary results in the following relations [6,47]:

$$u_r = \frac{k_{eff,f}\frac{\partial T}{\partial r}|_f - k_{eff,s}\frac{\partial T}{\partial r}|_s}{\varepsilon\rho_f L_{fs}} \quad (8a)$$

$$u_z = \frac{k_{eff,f}\frac{\partial T}{\partial z}|_f - k_{eff,s}\frac{\partial T}{\partial z}|_s}{\varepsilon\rho_f L_{fs}} \quad (8b)$$

where, herein, u_r and u_z are the components of the motion velocity of the interface boundary at the T_{fu} temperature. The governing equations are solved under the following boundary and initial conditions:

$$T = T_h, \vec{u} = 0 \quad \forall \quad r,z,t \quad \exists\ r = r_i, \quad 0 \leqslant z \leqslant L, \quad t \geqslant 0 \quad (9a)$$

$$T = T_c, \quad \vec{u} = 0 \quad \forall \quad r,z,t \quad \exists\ r = r_o, \quad 0 \leqslant z \leqslant L, \quad t \geqslant 0 \quad (9b)$$

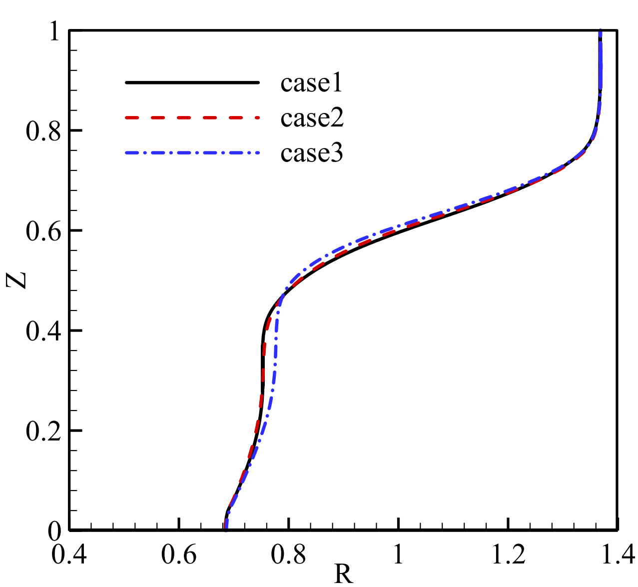

Fig. 2 The dependency of the melting-interface on the grid size when $Fo = 0.1$, $Ste = 0.012$, $Ra = 5 \times 10^6$ and $n = 0.6$ where x-direction shows the radius of pipe and Z-direction shows pipe's length.

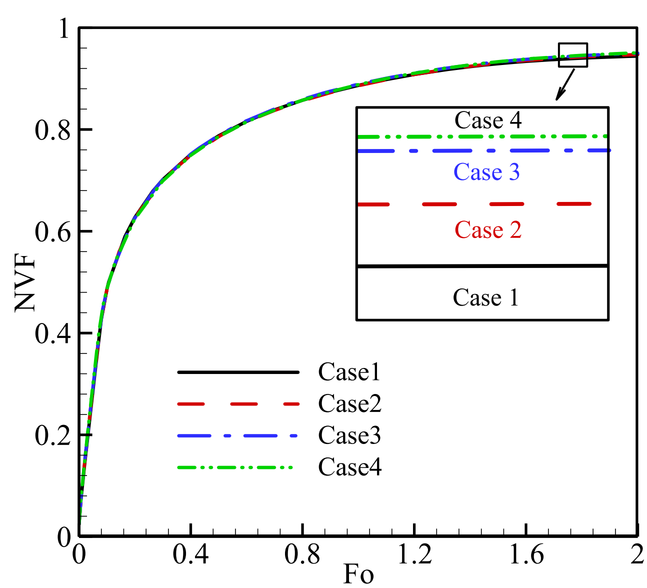

Fig. 3 The influence of various mesh cases on the melt volume fraction (NVF) when $Ste = 0.012$, $Ra = 5 \times 10^6$ and $n = 0.6$ as a function of the non-dimensional time (Fo).

$$\frac{\partial T}{\partial z} = 0, \quad \vec{u} = 0 \quad \forall \quad r, z, t \quad \exists \ z = 0, \quad r_i \leqslant r \leqslant r_o, \quad t \geqslant 0 \tag{9c}$$

$$\frac{\partial T}{\partial z} = 0, \quad \vec{u} = 0 \quad \forall \quad r, z, t \quad \exists \ z = L, \quad r_i \leqslant r \leqslant r_o, \quad t \geqslant 0 \tag{9d}$$

$$T = T_0, \ \vec{u} = 0 \ \ \forall \ r, \ z, \ t \ \exists \ r_i \leqslant r \leqslant r_o, \ 0 \leqslant z \leqslant L, t = 0 \tag{9e}$$

where $T_0 = T_c$.

The dimensionless variables transferring the equations and boundary conditions to dimensionless coordinates are as below:

$$R = \frac{r}{L}, Z = \frac{z}{L}, \vec{U} = \frac{\vec{u}L}{\alpha_f}, \theta = \frac{T - T_{fu}}{T_h - T_{fu}}, Fo = \frac{t\alpha_f}{L^2},$$
$$P = \frac{pL^2}{\rho\alpha_f^2}, \alpha_f = \frac{k_f}{(\rho C_p)_f} \tag{10}$$

Substituting the above relations for the dimensional variables in Eqs. (1), (2), (4), and (6) results in the equations below:

$$\nabla \cdot \vec{U} = 0 \tag{11}$$

$$\frac{1}{\varepsilon}\frac{\partial \vec{U}}{\partial Fo} + \frac{1}{\varepsilon^2}(\vec{U} \cdot \nabla)\vec{U} = \nabla \cdot \left[-PI + \frac{Pr\dot{G}^{n-1}}{\varepsilon}(\nabla\vec{U} + (\nabla\vec{U})^{tr}\right] - \frac{Pr}{Da}\dot{G}^{n-1}\vec{U} + PrRa\theta\vec{e}_z \tag{12}$$

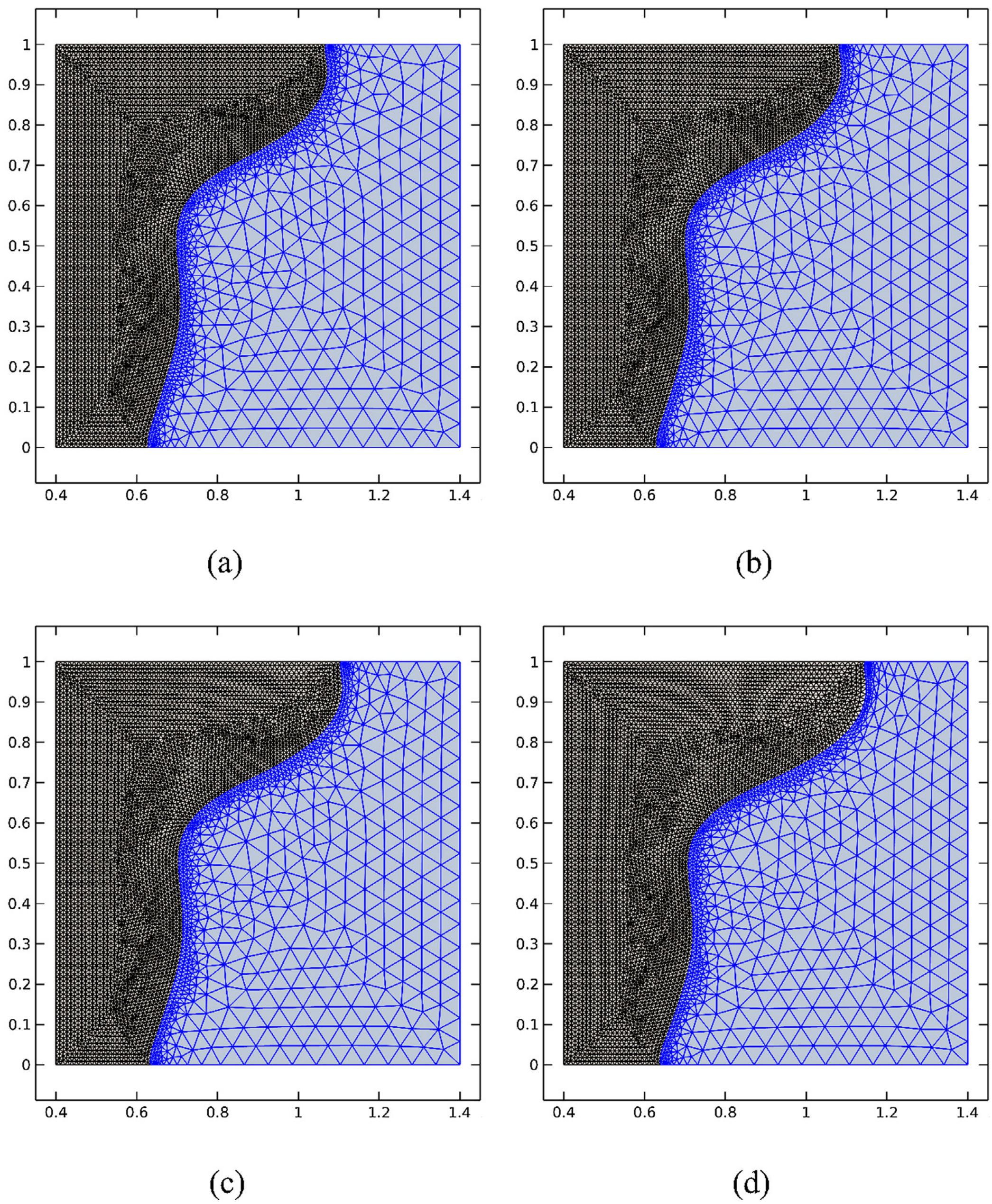

Fig. 4 The grid deformation during a stage of solution between two steps of re-meshing when (a) $Fo = 0.045$, (b) $Fo = 0.047$, (c) $Fo = 0.049$ and (d) $Fo = 0.053$.

$$\frac{(\rho C_p)_{eff,f}}{(\rho C_p)_f}\frac{\partial\theta}{\partial Fo}+\left(\vec{U}\cdot\nabla\theta\right)=\left(\nabla\cdot\left(\frac{k_{eff,f}}{k_f}\nabla\theta\right)\right) \tag{13}$$

$$\frac{(\rho C_p)_{eff,s}}{(\rho C_p)_f}\frac{\partial\theta}{\partial Fo}=\left(\nabla\cdot\left(\frac{k_{eff,s}}{k_f}\nabla\theta\right)\right) \tag{14}$$

The dimensionless numbers that appeared in the above equations, i.e., the Prandtl number (Pr), Rayleigh number (Ra), Darcy number (Da), and Stefan number (Ste), are as follows:

$$Pr=\frac{m}{\rho_f\alpha_f}\left(\frac{\alpha_f}{L^2}\right)^{n-1}=\frac{m}{\rho_f}\frac{\alpha_f^{n-2}}{L^{2n-2}},\ Ra=\frac{\rho_f g\beta_f(T_h-T_{fu})L^{2n+1}}{m\alpha_f^n},$$
$$Da=\frac{\kappa}{L^2},\ Ste=\frac{C_p(T_h-T_{fu})}{L_{fs}} \tag{15}$$

The velocity components of the phase change interface boundary in the dimensionless space can be defined as follows:

$$U_R=\frac{\left[k_{eff,f}\frac{\partial\theta}{\partial R}|_l-k_{eff,s}\frac{\partial\theta}{\partial R}|_s\right]Ste}{\varepsilon k_f} \tag{16a}$$

$$U_Z=\frac{\left[k_{eff,f}\frac{\partial\theta}{\partial Z}|_l-k_{eff,s}\frac{\partial\theta}{\partial Z}|_s\right]Ste}{\varepsilon k_f} \tag{16b}$$

On the interface boundary, the dimensionless temperature is zero. Also, the boundary and initial conditions at the dimensionless coordinates are:

$$\theta=1,\ \vec{U}=0\quad\forall\ R,\ Z,\ Fo\ \exists\ R=R_i,\ 0\leqslant Z\leqslant 1,\ Fo\geqslant 0 \tag{17a}$$

$$\theta=0,\vec{U}=0\quad\forall R,Z,Fo\ \exists\ R=R_o,0\leq Z\leq 1,Fo\geq 0 \tag{17b}$$

$$\frac{\partial\theta}{\partial Z}=0,\vec{U}=0\quad\forall R,Z,Fo\quad\exists Z=0,\quad R_i\leqslant R\leqslant R_o,\quad Fo\geqslant 0 \tag{17c}$$

$$\frac{\partial\theta}{\partial Z}=0,\quad\vec{U}=0\quad\forall R,Z,Fo\quad\exists Z=1,\quad R_i\leqslant R\leqslant R_o,\quad Fo\geqslant 0 \tag{17d}$$

$$\theta_0=\frac{T_0-T_{fu}}{T_h-T_{fu}}=0,\quad\vec{U}=0\ \forall\ R,Z,Fo\ \ \exists\ R_i\leq R\leq R_o,\ 0\leq Z\leq 1,\ \ Fo=0 \tag{17e}$$

The normalized volume fraction of molten substance is calculated using the relation below:

$$NVF=\frac{\int_0^1\int_{R_i}^{R_m}2\pi R\varepsilon(R)dRdZ}{\int_0^1\int_{R_i}^{R_o}2\pi R\varepsilon(R)dRdZ} \tag{18}$$

Energy balancing of a control surface on the inner pipe surface results in the following expression:

$$h(T_h-T_c)=-k_{eff}\frac{\partial T}{\partial r}\Big)_{r=r_i} \tag{19}$$

The transmission of the above-relation to the non-dimensional coordinates defines another parameter of interest, namely Nusselt number (Nu_z):

$$Nu_Z=\frac{hL}{k_f}=\left[\varepsilon+(1-\varepsilon)\frac{k_p}{k_f}\right]\frac{\partial\theta}{\partial R}\bigg|_{R=R_i} \tag{20}$$

Integrating the local Nusselt number Nu_z along the inner pipe surface, the mean Nusselt number (Nu_m) is evaluated as:

$$Nu_m=\int_o^1 Nu_z dz \tag{21}$$

3. Numerical method and grid examination

3.1. Grid check

The partial differential Eqs. (11)–(14) with the boundary constraints Eqs. (16) and (17) are solved using the Galerkin finite element approach. In this method, the PDEs are first transferred to a new form, namely weak form. The details of the utilized numerical method can be found in [48]. The constraint for the continuity equation is introduced as a penalty parameter (γ) in the momentum equations as described by Reddy [49]. In order to complete the numerical calculation, the grid independency of the resolution is studied. Hence, the computations are recalculated for several grid-sizes in the case of Pr = 60, Ste = 0.012, Ra = 5 × 10^6, n = 0.6, and ε = 0.9. Table 3

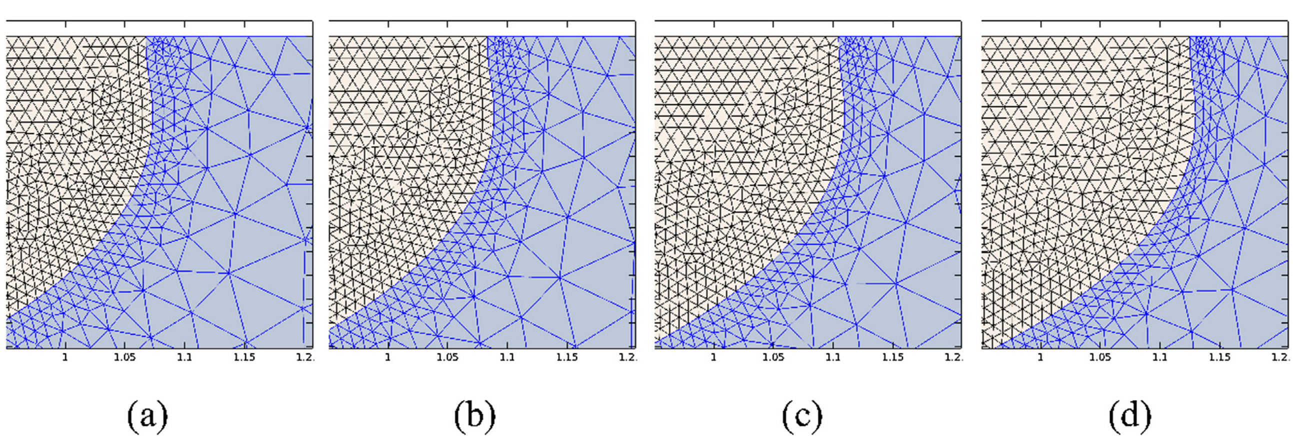

Fig. 5 Magnified view of grid deformation during a stage of solution between two steps of re-meshing which the originals are shown in Fig. 4.

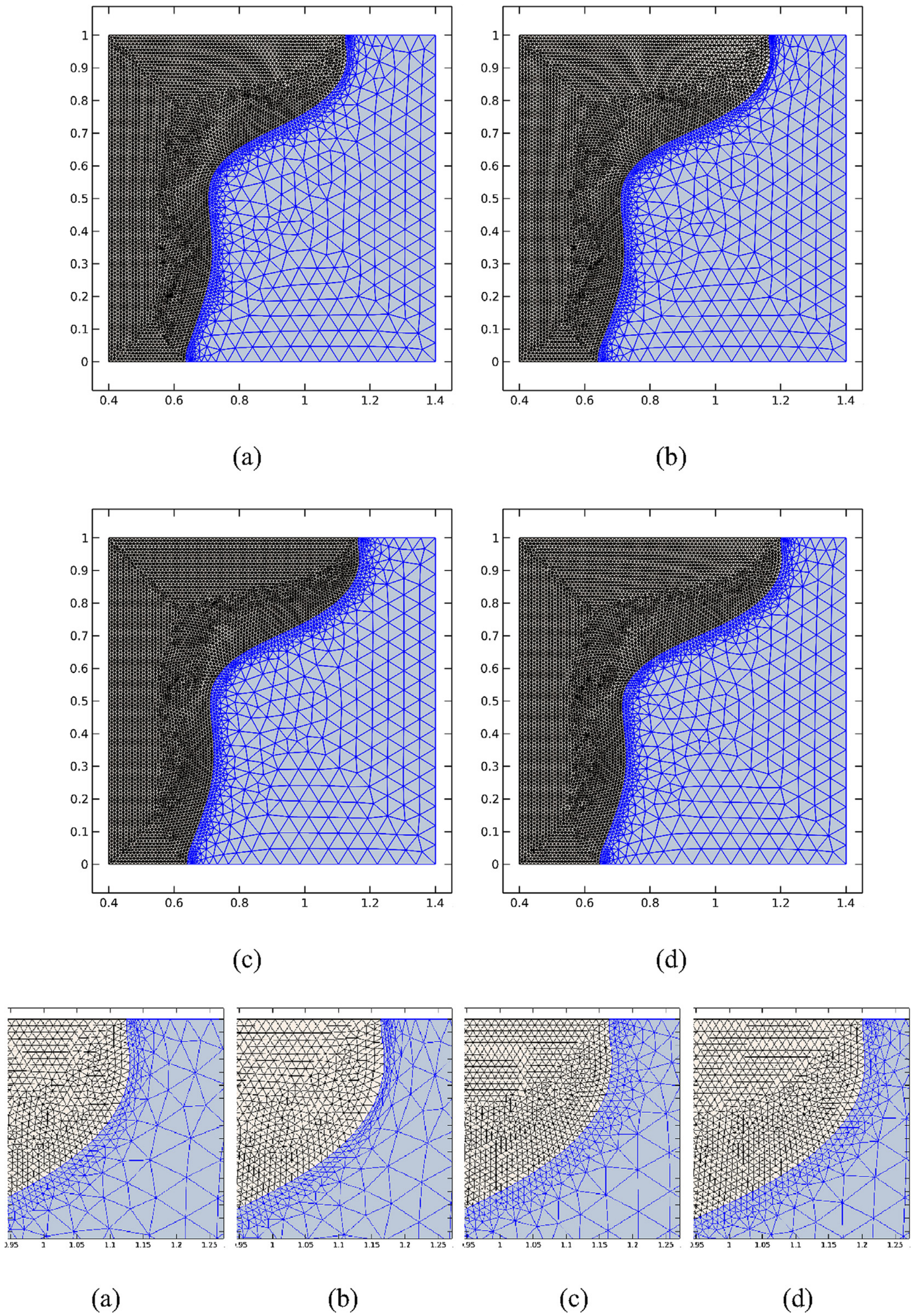

Fig. 6 Two sets of grid deformation just before and after re-meshing when (a) Fo = 0.051, (b) Fo = 0.055, (c) Fo = 0.05504 and (d) Fo = 0.059.

demonstrates the utilized grids-sizes. The liquid fraction and melting interface for different grid size is depicted in Figs. 2 and 3. The results show that the grid size of case 3 can provide acceptable accuracy. Therefore, the grid size of case 3 is selected to carry out the results of the present study.

The technique of re-meshing during the melting process is utilized to satisfy the precision of the results. Figs. 4 and 5 shows the deformable grid pattern between two steps of re-meshing during a step of the solution. As shown in Figs. 4 and 5, the grid pattern moves and changes by various Fourier number. Fig. 6

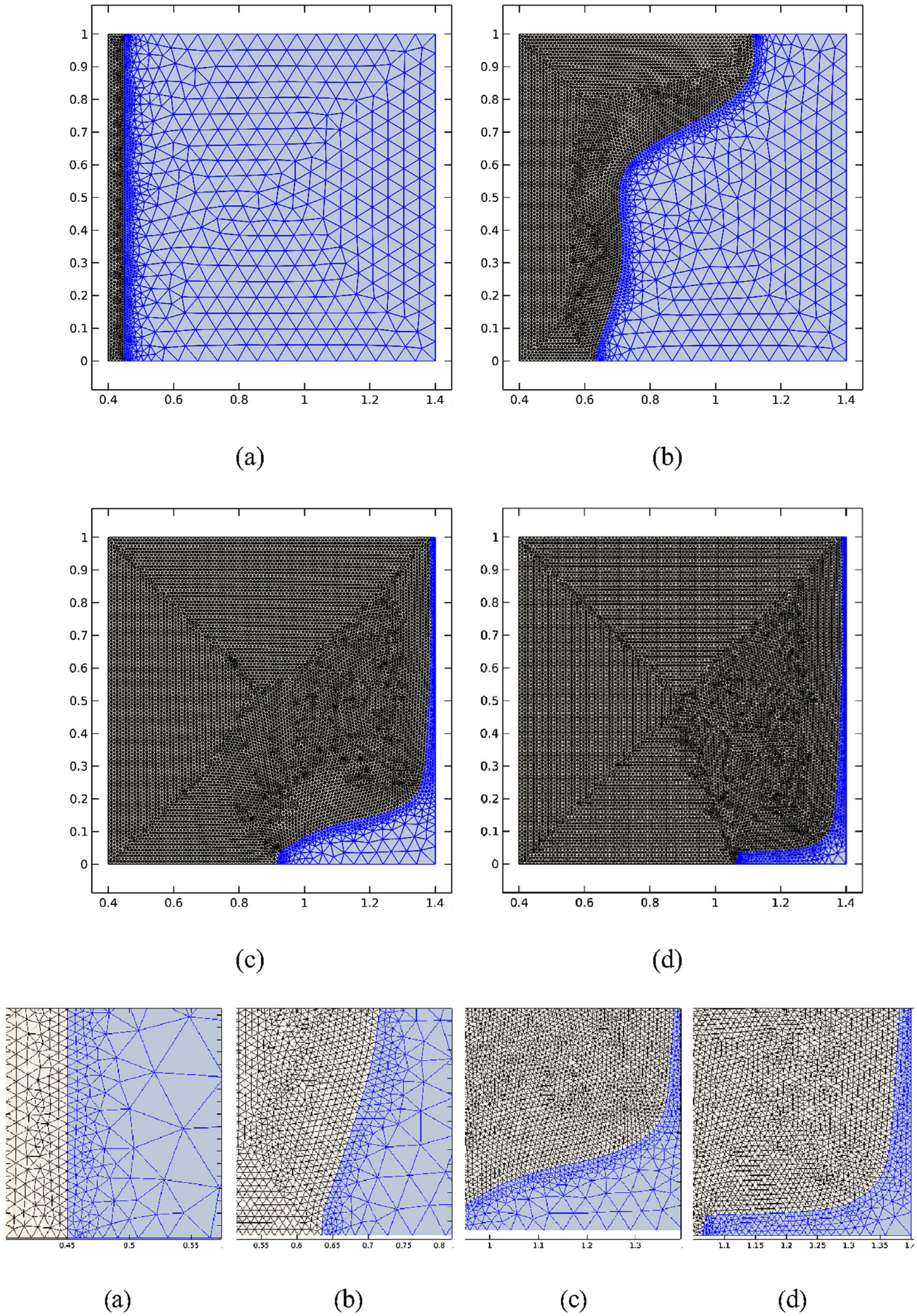

Fig. 7 View of the utilized grid in different stages of the solution when (a) $Fo = 0$, (b) $Fo = 0.05$, (c) $Fo = 1$ and (d) $Fo = 2$.

depicts the grid patterns just after and before a re-meshing step. The dominant heat transfer mechanism in the porous medium is diffusion, and because of the low thermal resistance in the porous medium, there are no significant temperature gradients in the porous medium. Based on Fig. 6, it is clear that the temperature gradient in the solid region is almost zero, as the temperature of the phase change interface and that of the cold wall are identical. Hence, the grids in the melted liquid part have a smaller size than the solid region. So, to reach accurate results, the grid pattern changes alternately. Fig. 7 illustrated the process of full melting during the non-dimensional time Fo. It is shown that the grid pattern moves and changes clearly.

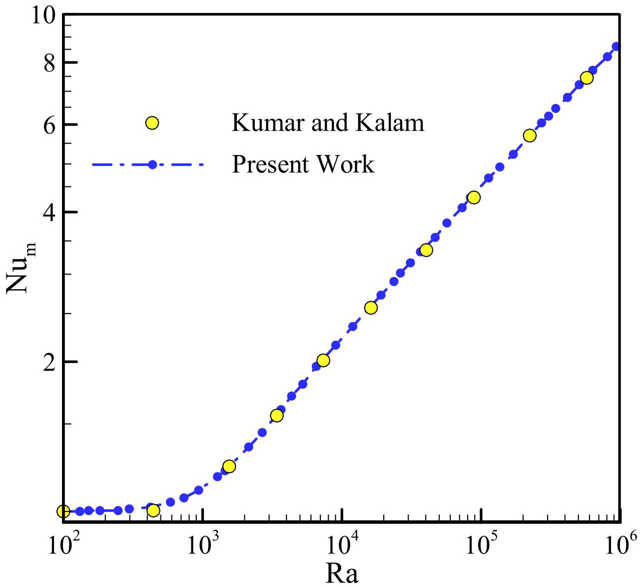

Fig. 8 Average Nusselt number against Rayleigh number of the current study (points) and Kumar and Kamal (dash-dot) [45].

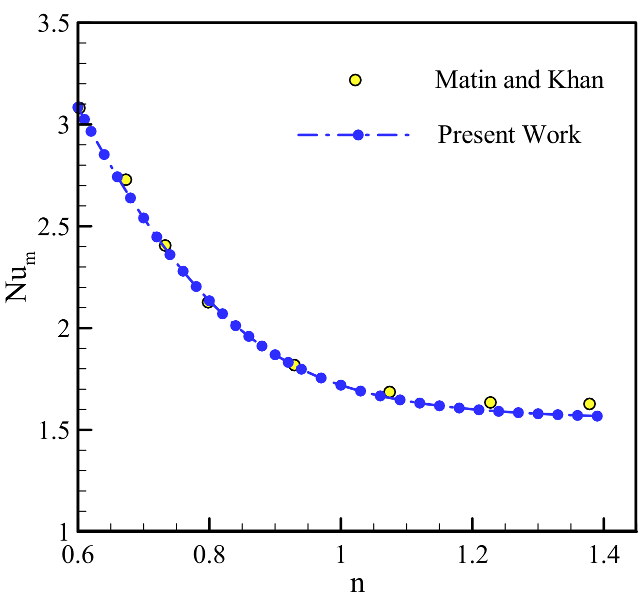

Fig. 9 Average Nusselt number against power-law index n of the current study (dash-dot) and Matin and Khan (points) [50].

3.2. Comparison with previous works

The correctness and accuracy of the numerical outcomes can be verified and validated through other numerical and experimental results, respectively, reported in [45,50–53]. As a validation of the natural convection inside a vertical coaxial pipe, Kumar and Kalam's investigation [45] has been studied. In the work of Kumar and Kalam [45], the inner pipe maintained at a higher temperature compared to the outer one, and the bottom and upper walls were perfectly insulated. The space between the outer and inner pipes was occupied with air as a Newtonian fluid. Fig. 8 shows a comparison of the outcomes of the present study with the outcomes of Kumar and Kalam's

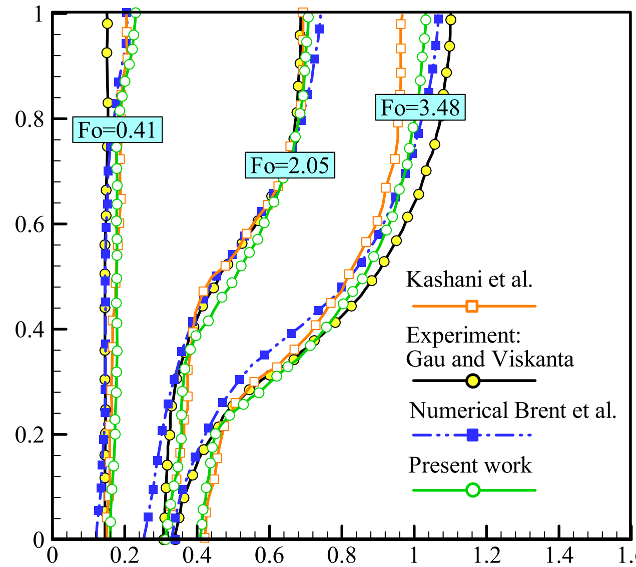

Fig. 10 Comparison between the melting front obtained by the current work and the one reported in [51].

study [45]. The constant parameters for this evaluation are $Pr = 0.71$, $L/(r_o - r_i) = 1$, and $r_o/r_i = 2$. The comparison shows that there is a desirable agreement between the results.

To validate the natural convection of a non-Newtonian power-law fluid in an enclosure, the study of Matin and Khan [50] is re-stimulated through the utilized code in the present study. Matin and Khan [50] studied the free heat transfer of a non-Newtonian power-law fluid in annuli of the horizontal cylinders with the hot and cold temperatures at the inner and outer cylinders. For a case of non-Newtonian fluid with $Pr = 10$ and $Ra = 10^3$, a comparison between the average Nusselt numbers of the present study and those of [50] is displayed in Fig. 9 for different values of the power-law index. As shown, the results are in excellent agreement.

For validation of the melting process, comparisons between the melting fronts obtained in the present study and those presented in [51] are conducted, as depicted in Fig. 10. The studied problem physics in [51] included a square cavity with the horizontal insulated walls. However, the left and right of the cavity are subjected to higher and lower temperatures. The pure gallium was selected as the Newtonian phase change substance. The dimensionless parameters based on the thermophysical properties of the PCM, the thermal boundary conditions, and the geometrical characteristics were such that $Pr = 0.0216$, $Ra = 6 \times 10^5$, and $Ste = 0.039$. As shown in Fig. 10, the results of the current work are in good agreement with Gau and Viskanta [51] and the theoretical works of Brent et al. [54] and Kashani et al. [55].

As the last validation, the heat transfer rates through a porous medium obtained in the current work are compared to the works [52,53]. The fluid flowing inside the porous medium was water with $Pr = 6.2$. Evidently, the outcomes are consistent with the findings reported in [52,53]. As the comparisons conducted in Figs. 8–10 and Table 4 demonstrate that the numerical modeling has correctly been performed, and the utilized code is reliable.

Table 4 The average Nusselt number in a triangular cavity filled with a porous medium.

$Ra \times Da$	Sun and Pop al [52]	Sheremet et al. [53]	Present work
500	9.66	9.65	9.64
1000	13.9	14.05	13.96

4. Results and discussion

This section deals with the results obtained for the natural convection of a non-Newtonian PCM inside a porous medium. The default parameters here are set as $Pr = 60$, $Da = 10^{-4}$, $\varepsilon = 0.9$ and $Ra = 5 \times 10^6$, while the other parameters can be varied such as $n = 0.6\text{–}1.0$ and $Ste = 0.010\text{–}0.014$. Fig. 11 shows the deformed mesh pattern during the melting phase change for $Ra = 5 \times 10^6$, $Ste = 0.12$, $Fo = 0.05$, and for different values of the non-Newtonian index n. As mentioned, the simulation code employs a re-meshing technique to monitor and control the accuracy of the outcomes during the mesh evolutions. As shown in Fig. 11, the utilized grid in this region has a larger size in comparison with the liquid side. For example, as shown in Table 3, just in case 3, the maximum size of the grid in the solid region is five times larger than the grid size in the liquid region. Also, the temperature of the cold wall and the melting interface is the same in the solid region, so no temperature gradient is expected in the solid region.

Fig. 12 displays the evaluations of the deformed patterns during the melting phase change for $Ra = 5 \times 10^6$, $n = 0.6$, $Fo = 0.05$, and for various values of Stefan number (Ste). It is shown that for the same value of Fo, raising Ste increases

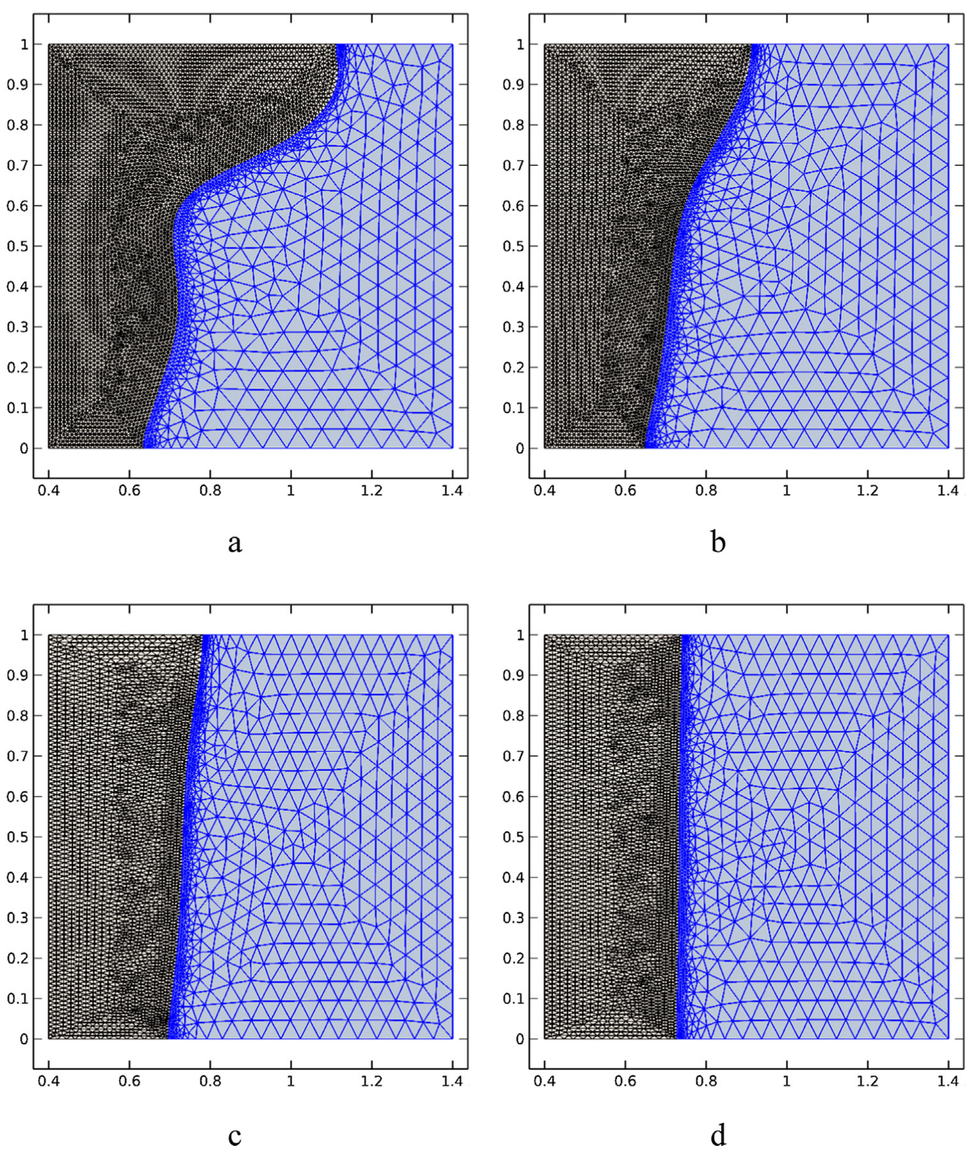

Fig. 11 A view of the mesh evolutions during the melting phase change when $Ste = 0.12$, $Fo = 0.05$ and (a) $n = 0.6$, (b) $n = 0.7$, (c) $n = 0.8$ and (d) $n = 1$.

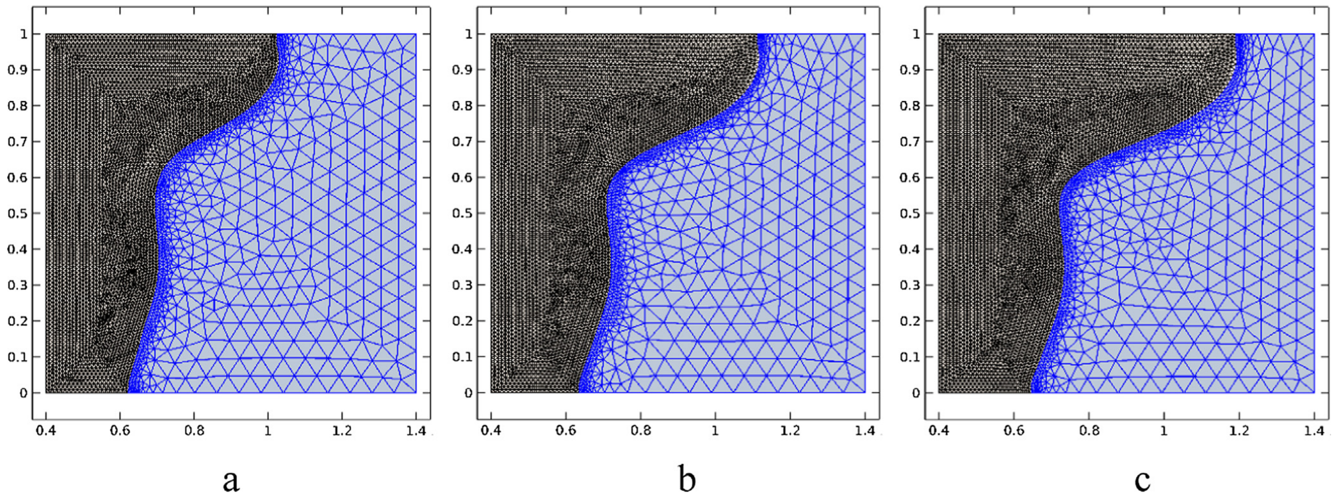

Fig. 12 A view of the mesh evolutions during the melting phase change when n = 0.6, *Fo* = 0.05, *Ra* = 5 × 10^6 and (a) *Ste* = 0.01, (b) *Ste* = 0.012 and (c) *Ste* = 0.014.

the depth of the melting interface and the melted liquid region. In Figs. 11 and 12, the black mesh on the left side is the liquid region, and the blue mesh on the right side is the solid region.

Figs. 13–15 show streamlines, isotherm patterns, and the melting interface of the melted liquid for different values of *Ste* and *n* when *Ra* = 5 × 10^6. It is clear that varying *Ste*

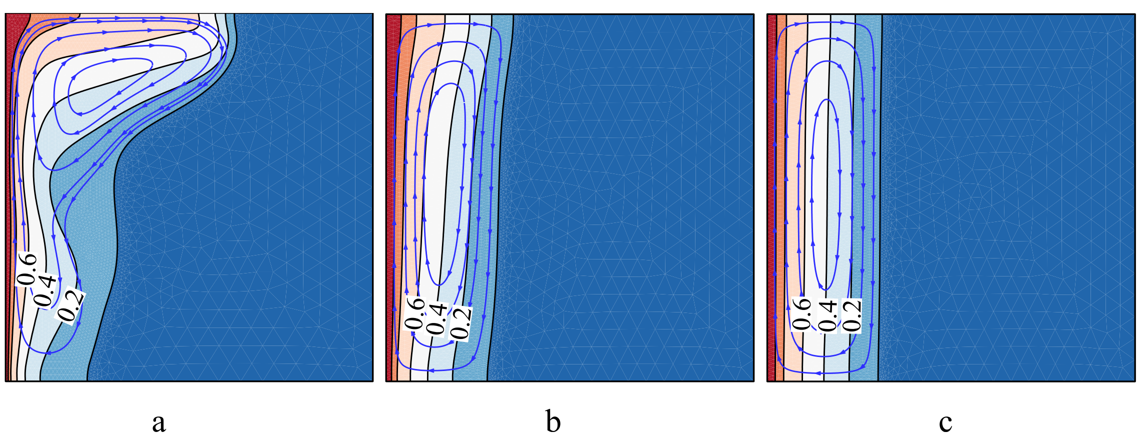

Fig. 13 Display of streamlines and isotherms for *Ra* = 5 × 10^6, *Fo* = 0.05 and *Ste* = 0.010 when (a) *n* = 0.6, (b) *n* = 0.8 and (c) *n* = 1.

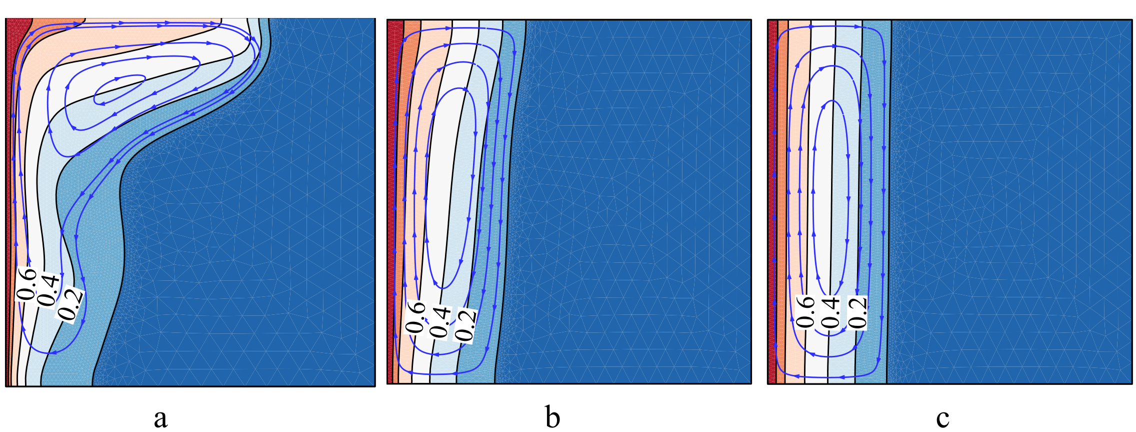

Fig. 14 Display of streamlines and isotherms for *Ra* = 5 × 10^6, *Fo* = 0.05 and *Ste* = 0.012 when (a) *n* = 0.6, (b) *n* = 0.8 and (c) *n* = 1.

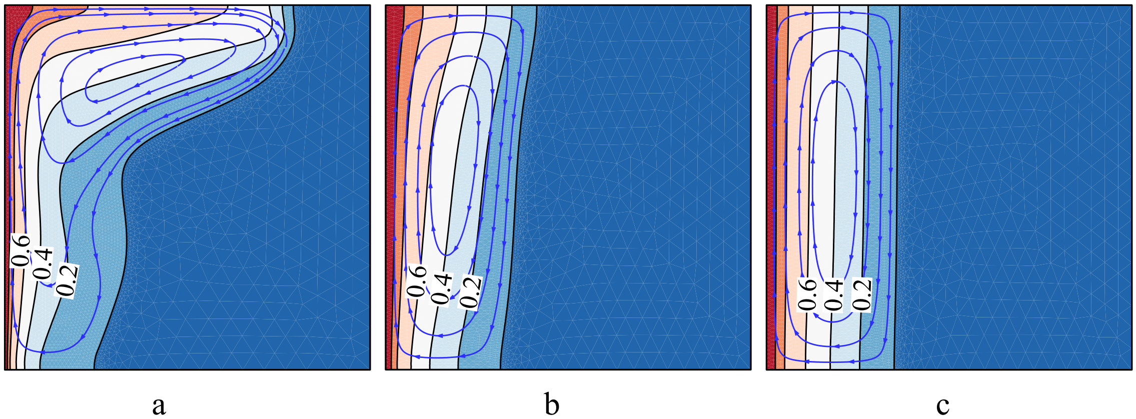

Fig. 15 Display of streamlines and isotherms for $Ra = 5 \times 10^6$, $Fo = 0.05$ and $Ste = 0.014$ when (a) $n = 0.6$, (b) $n = 0.8$ and (c) $n = 1$.

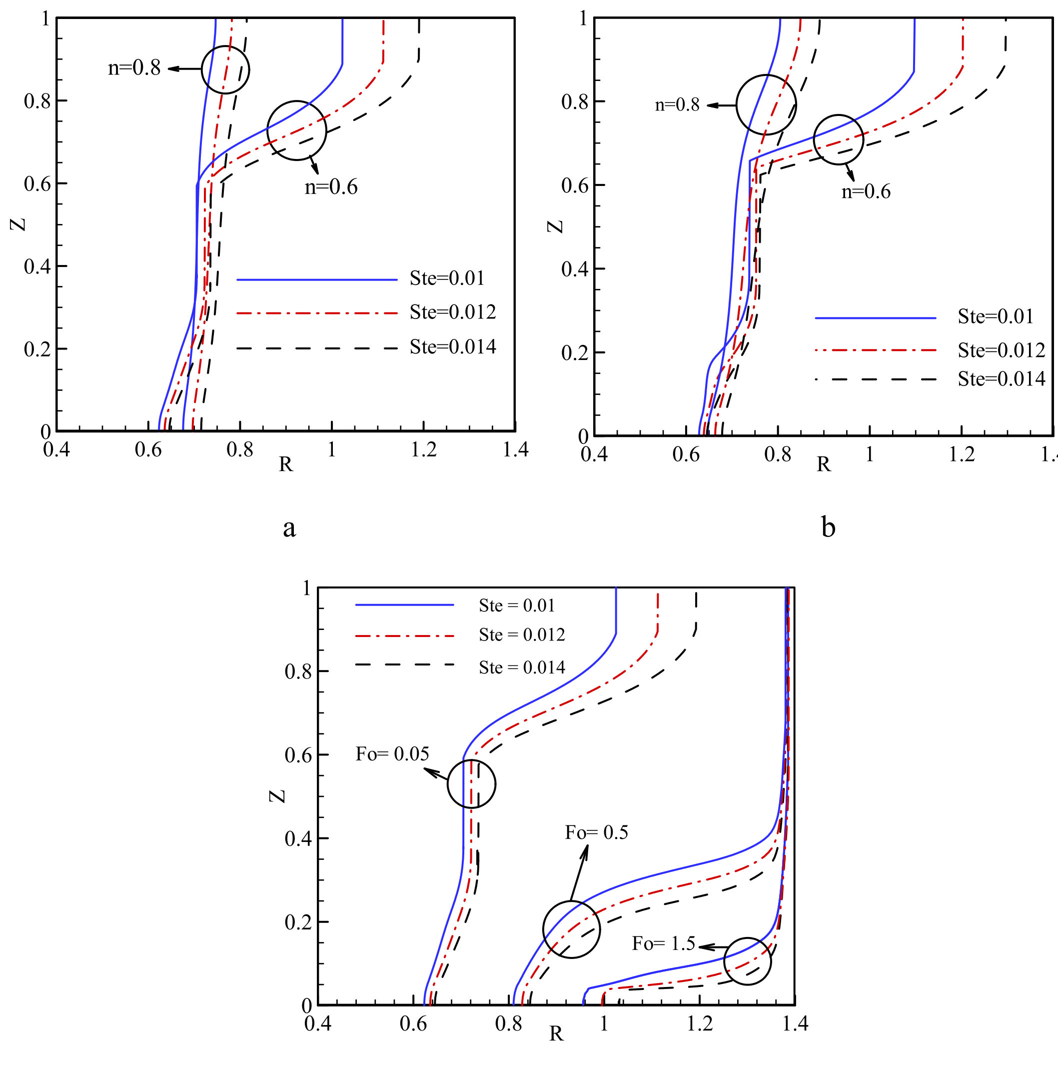

Fig. 16 The melting front interface for three different Stefan numbers and (a) $Fo = 0.05$, $n = 0.6$ and 0.8, and $Ra = 5 \times 10^6$, (b) $Fo = 0.05$, $n = 0.6$ and 0.8 and, $Ra = 10^7$, (c) $n = 0.6$ and $Fo = 0.05$, 0.5 and 1.5, and $Ra = 5 \times 10^6$.

and n considerably changes the streamlines and temperature contour in the pipe. When n decreases, the melted liquid space and the melting-front further advance toward the solid region. The streamline patterns are entirely affected by the variation of n. As shown in the figures, growing Ste increases the depth of the melting region and the melting ratio.

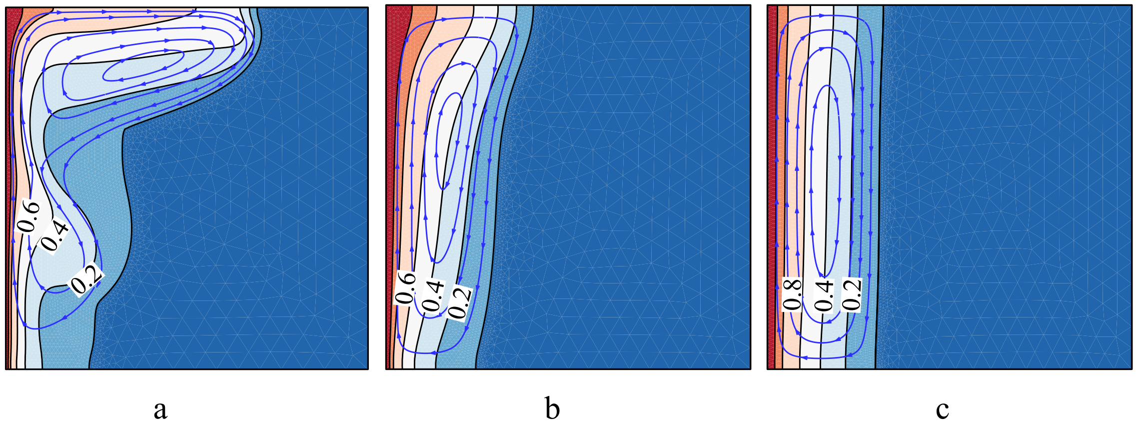

Fig. 17 The contours of streamlines and isotherms for $Ra = 10^7$, $Fo = 0.05$ and $Ste = 0.010$ when (a) $n = 0.6$, (b) $n = 0.8$ and (c) $n = 1$.

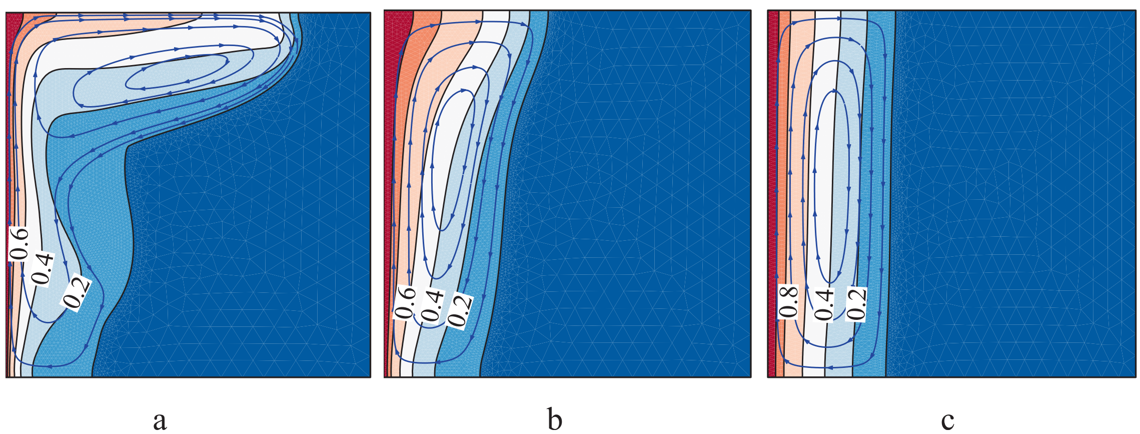

Fig. 18 The contours of streamlines and isotherms for $Ra = 10^7$, $Fo = 0.05$ and $Ste = 0.012$ when (a) $n = 0.6$, (b) $n = 0.8$ and (c) $n = 1$.

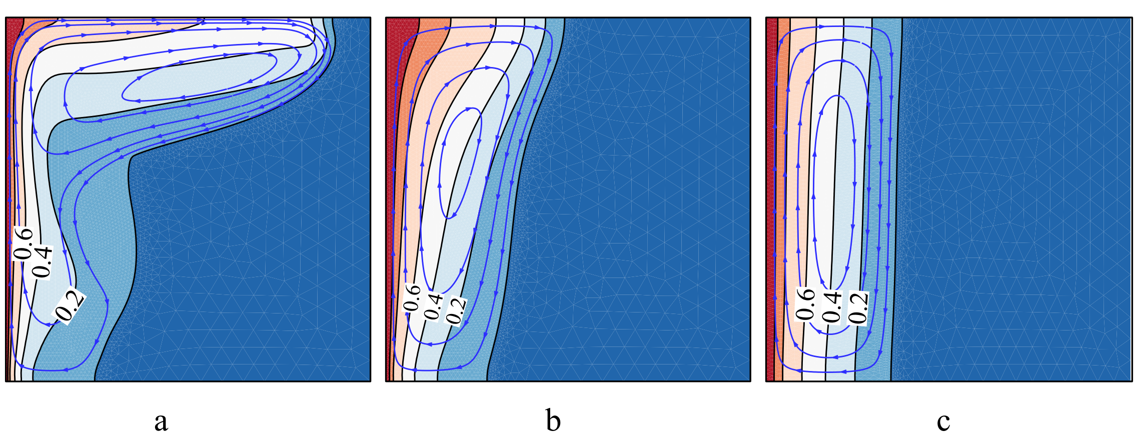

Fig. 19 The contours of streamlines and isotherms for $Ra = 10^7$, $Fo = 0.05$ and $Ste = 0.014$ when (a) $n = 0.6$, (b) $n = 0.8$ and (c) $n = 1$.

In the case of $n = 1$, i.e., for a Newtonian fluid, the streamlines are circular while the isotherms are almost straight, and a symmetrical pattern can be observed. By decreasing n, the fluid exhibits a non-Newtonian behavior, and the streamlines lose their circularity and deflect toward the cold wall. In the case $n = 0.6$, there is no symmetry in the streamlines. In fact, the dynamic viscosity is a function of the shear rate and, therefore, an asymmetry in the streamlines arises. Following the remark-

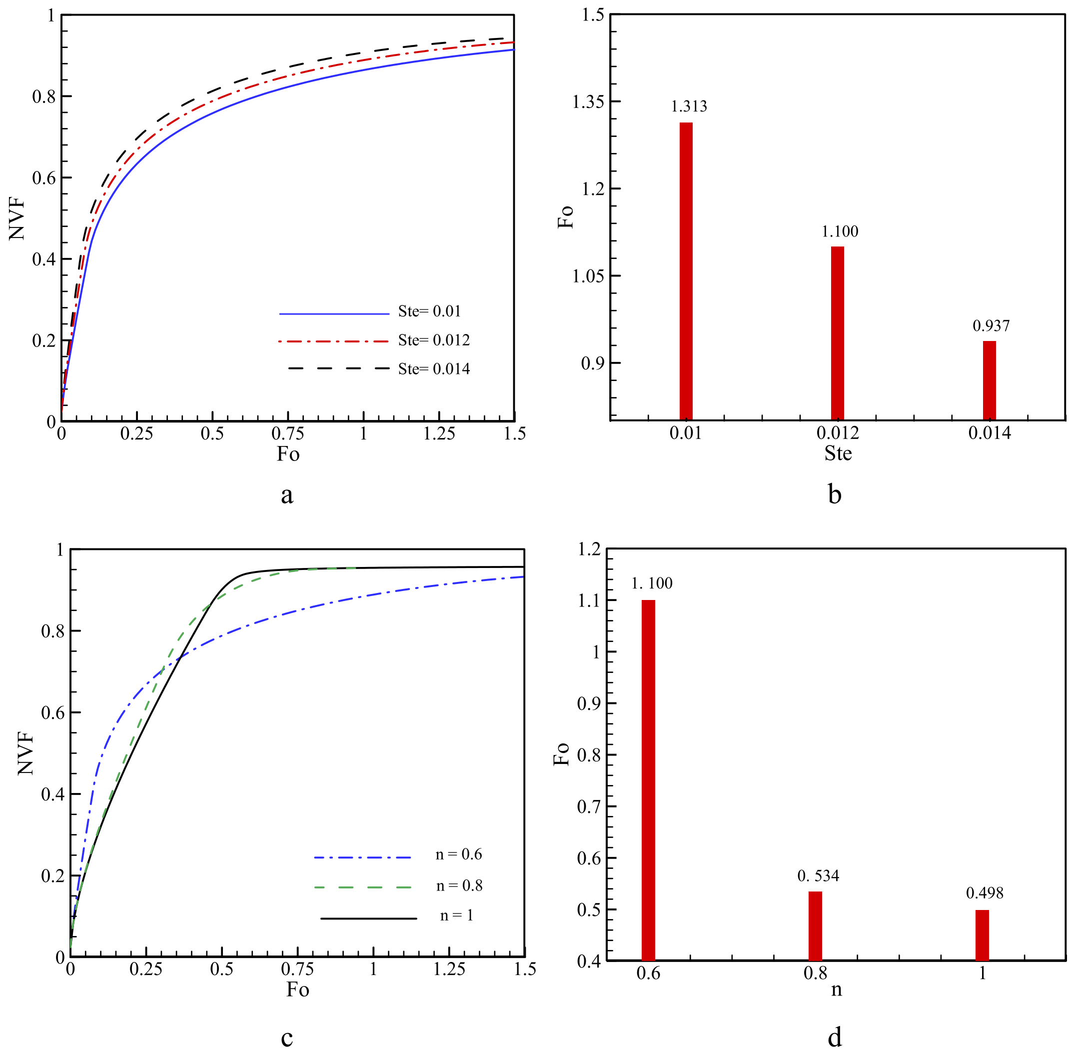

Fig. 20 Time history of the melting volume fraction and the time of a complete melting; (a) Time history of the melting volume fraction for different values of *Ste* when $n = 0.6$, (b) the required time of a complete melt for various values of Stefan Number when $n = 0.6$, (c) Time history of the melting volume fraction as a function of *n* when $Ste = 0.012$, (d) the required time of a complete melt for various values of *n* when $Ste = 0.012$.

able change in the streamlines, the temperature distribution is also affected. As shown in Figs. 13–15(a), in the case of $n = 0.6$, the isotherm lines deflect toward the cold wall. However, for the other two values of n, the isotherms remain almost straight.

The effect of *Ste* and *Fo* on the melting process is investigated by following the variation of the melting interface depicted in Fig. 16. When $Fo = 0.05$, the variation of *Ste* has a noticeable effect on the melted liquid space, for the different values of *n*. Increasing *Ste* lowers the depth of melted liquid. Moreover, using higher values of *n* and *Ra* affects the depth of the melting interface and increases the melted liquid region. In fact, by increasing *Ra*, the velocity rises, and the dynamic viscosity of fluid decreases, thus enhancing the convective heat transfer. In order to investigate the effect of *n* on the melted liquid region and the melting interface, Fig. 16 (a) and (b) illustrate the melted front surface for three different values of *n*. As mentioned previously, increasing *n* affects the melted region and reduces the depth of the melting interface.

Figs. 17–19 show the effect of *Ra* on the melted liquid space and the advancement of the melting front interface. Raising *Ra* increases the advancement of the melting front and the melted liquid space. This is since the thermal resistance weakens by the increase of *Ra*, as a high value of *Ra* means that the buoyancy force is dominant compared to the vicious one and, therefore, the convective heat transfer is the dominant mechanism in the melting process. It can be also seen that *n* has a significant impact on the depth of the melting interface. By decreasing the value of *n* from $n = 1$, representing the Newtonian fluid, to $n = 0.6$, a non-newtonian one, the depth of melting interface is dramatically increased, especially for $Ste = 0.014$.

Fig. 20(a) and (c) show the effect of *n* and *Ste* on the variation of the liquid fraction as a function of *Fo* when $Ra = 5 \times 10^6$. It can be seen that increasing *Ste* raises the liquid fraction. Complete melting is reached earlier when *Ste* is increased. However, for low values of *Fo*, the variation of *Ste* does not have a noticeable effect on the liquid fraction. On the other hand, the variation of *n* affects the liquid fraction dramatically.

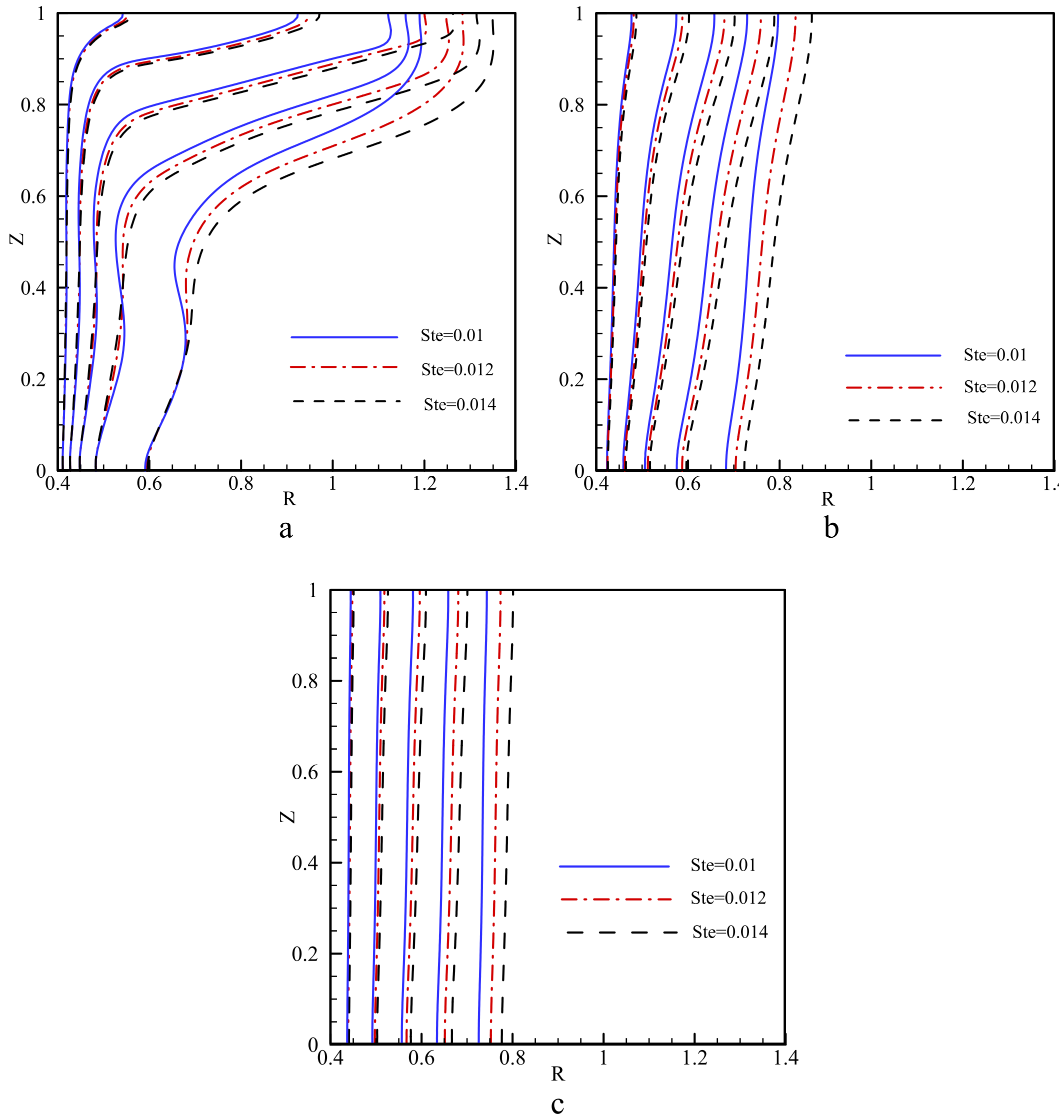

Fig. 21 The contours of isotherms for $Ra = 5 \times 10^6$, $Fo = 0.07$ and different value of Stefan number when (a) $n = 0.6$, (b) $n = 0.8$ and (c) $n = 1$.

As shown in Fig. 20(b) and (d), raising n from 0.6 to 0.8 significantly reduces the required time for reaching a complete melting. It is shown that the required time for full melting is at its highest when $n = 0.6$ and $Ste = 0.010$ for $Fo = 1.313$, while it is minimum when $n = 1$ and $Ste = 0.012$ for $Fo = 0.498$.

Fig. 21 depicts the isotherm patterns for different values of Ste and n. As previously mentioned, it is clear that n has a significant effect on the liquid fraction and the advancement of the melted interface. This means that increasing n reduces the depth of the melted surface. In addition, in the case of a Newtonian fluid ($n = 1$), the isotherms are almost straight lines, indicating a conduction dominated heat transfer during the process. By decreasing n from 1 to 0.6, the share of conduction in heat transfer is reduced while the convective transfer is enhanced.

Fig. 22 illustrates the variation of the local Nusselt number (Nu_Z) at the hot wall ($R = R_i$) for $n = 0.6$, $Ra = 5 \times 10^6$ and for different values of Ste. It is shown that using a higher value of Ste decreases the local Nusselt number slightly. For low values of Fo ($Fo < 0.025$), the Nusselt number dramatically decreases as a function of Fo. When Fo increases, for all the values of Ste, Nu_Z remains almost steady and unchanged, with a slight increase for lower values of Ste. Indeed, a higher value of Ste reduces the latent heat of the PCM. As a result, the contribution of the PCM phase change to the overall heat transfer decreases, and Nu_Z is reduced.

5. Conclusion

The present paper provides a numerical investigation of the melting of a non-Newtonian Phase Change Material (PCM) in the porous space between two coaxial pipes. The inner and outer pipes are kept at the high and low temperatures of T_h and T_c, respectively. The other surfaces of the coaxial pipe

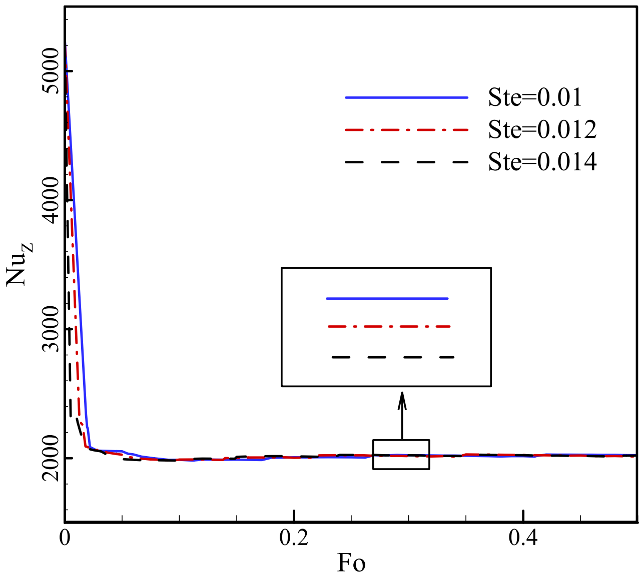

Fig. 22 The Nusselt number (Nu_Z) at the inner radius ($R = R_i$) when $n = 0.6$, $Ra = 5 \times 10^6$ and different value of Stefan number.

are insulated. The gravity acceleration is imposed along the central line of the pipe. The weakened forms of the governing equations are solved using the finite element method implemented in Arbitrary Eulerian-Lagrangian (ALE) moving grid technique. Tracking the interface of the solid–liquid of the non-Newtonian PCM is conducted through the Stefan condition. The grid check is performed to ensure the independence of the numerical results from the grid size. The numerical outcomes are verified by comparison of the obtained results to those presented in several published works. The main outcomes of the simulations indicate that the Stefan number and the power-law index can drastically affect the melting progress and the required time of a full-melting. The full-melting time can be declined until 54% as the power-law index decreases from 1 to 0.6.

Declaration of Competing Interest

The authors declare that they have no known competing financial interests or personal relationships that could have appeared to influence the work reported in this paper.

References

[1] Y. Tao, Y.-L. He, A review of phase change material and performance enhancement method for latent heat storage system, Renew. Sustain. Energy Rev. 93 (2018) 245–259.
[2] Y. Lin, Y. Jia, G. Alva, G. Fang, Review on thermal conductivity enhancement, thermal properties and applications of phase change materials in thermal energy storage, Renew. Sustain. Energy Rev. 82 (2018) 2730–2742.
[3] S. Demirbağ, S.A. Aksoy, Encapsulation of phase change materials by complex coacervation to improve thermal performances and flame retardant properties of the cotton fabrics, Fibers Polym. 17 (3) (2016) 408–417.
[4] A. Hajjar, S. Mehryan, M. Ghalambaz, Time periodic natural convection heat transfer in a nano-encapsulated phase-change suspension, Int. J. Mech. Sci. (2019) 105243.
[5] M. Ghalambaz, A.J. Chamkha, D. Wen, Natural convective flow and heat transfer of Nano-Encapsulated Phase Change Materials (NEPCMs) in a cavity, Int. J. Heat Mass Transfer 138 (2019) 738–749.
[6] M. Ghalambaz, T. Groşan, I. Pop, Mixed convection boundary layer flow and heat transfer over a vertical plate embedded in a porous medium filled with a suspension of nano-encapsulated phase change materials, J. Mol. Liquids 293 (2019) 111432.
[7] C.J. Ho, J. Gao, Preparation and thermophysical properties of nanoparticle-in-paraffin emulsion as phase change material, Int. Commun. Heat Mass Transfer 36 (5) (2009) 467–470.
[8] M. Sheikholeslami, O. Mahian, Enhancement of PCM solidification using inorganic nanoparticles and an external magnetic field with application in energy storage systems, J. Clean. Prod. 215 (2019) 963–977.
[9] N.S. Bondareva, B. Buonomo, O. Manca, M.A. Sheremet, Heat transfer inside cooling system based on phase change material with alumina nanoparticles, Appl. Therm. Eng. 144 (2018) 972–981.
[10] N.S. Bondareva, B. Buonomo, O. Manca, M.A. Sheremet, Heat transfer performance of the finned nano-enhanced phase change material system under the inclination influence, Int. J. Heat Mass Transfer 135 (2019) 1063–1072.
[11] W. Alshaer, S. Nada, M. Rady, C. Le Bot, E.P. Del Barrio, Numerical investigations of using carbon foam/PCM/Nano carbon tubes composites in thermal management of electronic equipment, Energy Convers. Manage. 89 (2015) 873–884.
[12] K. Ermis, A. Erek, I. Dincer, Heat transfer analysis of phase change process in a finned-tube thermal energy storage system using artificial neural network, Int. J. Heat Mass Transfer 50 (15–16) (2007) 3163–3175.
[13] Z. Li, Z.-G. Wu, Numerical study on the thermal behavior of phase change materials (PCMs) embedded in porous metal matrix, Solar Energy 99 (2014) 172–184.
[14] R. Baby, C. Balaji, Thermal optimization of PCM based pin fin heat sinks: an experimental study, Appl. Therm. Eng. 54 (1) (2013) 65–77.
[15] M. Sheikholeslami, R.-U. Haq, A. Shafee, Z. Li, Heat transfer behavior of nanoparticle enhanced PCM solidification through an enclosure with V shaped fins, Int. J. Heat Mass Transfer 130 (2019) 1322–1342.
[16] N.S. Bondareva, M.A. Sheremet, Conjugate heat transfer in the PCM-based heat storage system with finned copper profile: Application in electronics cooling, Int. J. Heat Mass Transfer 124 (2018) 1275–1284.
[17] Z.A. Qureshi, H.M. Ali, S. Khushnood, Recent advances on thermal conductivity enhancement of phase change materials for energy storage system: a review, Int. J. Heat Mass Transfer 127 (2018) 838–856.
[18] A. Siahpush, J. Obrien, J. Crepeau, Phase change heat transfer enhancement using copper porous foam, J. Heat Transfer 130 (8) (2008) 082301.
[19] C. Zhao, W. Lu, Y. Tian, Heat transfer enhancement for thermal energy storage using metal foams embedded within phase change materials (PCMs), Solar Energy 84 (8) (2010) 1402–1412.
[20] X. Xiao, P. Zhang, M. Li, Preparation and thermal characterization of paraffin/metal foam composite phase change material, Appl. Energy 112 (2013) 1357–1366.
[21] X. Xiao, P. Zhang, M. Li, Effective thermal conductivity of open-cell metal foams impregnated with pure paraffin for latent heat storage, Int. J. Therm. Sci. 81 (2014) 94–105.
[22] K. Lafdi, O. Mesalhy, S. Shaikh, Experimental study on the influence of foam porosity and pore size on the melting of phase change materials, J. Appl. Phys. 102 (8) (2007) 083549.
[23] Z. Chen, D. Gao, J. Shi, Experimental and numerical study on melting of phase change materials in metal foams at pore scale, Int. J. Heat Mass Transfer 72 (2014) 646–655.

[24] Y. Tian, C. Zhao, Thermal and exergetic analysis of metal foam-enhanced cascaded thermal energy storage (MF-CTES), Int. J. Heat Mass Transfer 58 (1–2) (2013) 86–96.
[25] M. Jourabian, M. Farhadi, A.R. Darzi, Constrained ice melting around one cylinder in horizontal cavity accelerated using three heat transfer enhancement techniques, Int. J. Therm. Sci. 125 (2018) 231–247.
[26] M. Jourabian, A.A.R. Darzi, D. Toghraie, O. Ali Akbari, Melting process in porous media around two hot cylinders: numerical study using the lattice Boltzmann method, Physica A: Stat. Mech. Appl. 509 (2018) 316–335.
[27] B.V.S. Dinesh, A. Bhattacharya, Effect of foam geometry on heat absorption characteristics of PCM-metal foam composite thermal energy storage systems, Int. J. Heat Mass Transfer 134 (2019) 866–883.
[28] F. Wang, W. Lin, Z. Ling, X. Fang, A comprehensive review on phase change material emulsions: fabrication, characteristics, and heat transfer performance, Solar Energy Mater. Solar Cells 191 (2019) 218–234.
[29] N.S. Bondareva, M.A. Sheremet, Flow and heat transfer evolution of PCM due to natural convection melting in a square cavity with a local heater, Int. J. Mech. Sci. 134 (2017) 610–619.
[30] M.S. Astanina, M. Sheremet, C.J. Umavathi, Unsteady natural convection in a partially porous cavity having a heat-generating source using local thermal non-equilibrium model, Int. J. Numer. Methods Heat Fluid Flow (2018).
[31] S. Mehryan, M.A. Sheremet, M. Soltani, M. Izadi, Natural convection of magnetic hybrid nanofluid inside a double-porous medium using two-equation energy model, J. Mol. Liquids 277 (2019) 959–970.
[32] A.I. Alsabery, R. Mohebbi, A.J. Chamkha, I. Hashim, Effect of local thermal non-equilibrium model on natural convection in a nanofluid-filled wavy-walled porous cavity containing inner solid cylinder, Chem. Eng. Sci. 201 (2019) 247–263.
[33] A.K. Asl, S. Hossainpour, M. Rashidi, M. Sheremet, Z. Yang, Comprehensive investigation of solid and porous fins influence on natural convection in an inclined rectangular enclosure, Int. J. Heat Mass Transfer 133 (2019) 729–744.
[34] M.A. Sheremet, I. Pop, Effect of local heater size and position on natural convection in a tilted nanofluid porous cavity using LTNE and Buongiorno's models, J. Mol. Liquids 266 (2018) 19–28.
[35] A. Dogonchi, M. Sheremet, D. Ganji, I. Pop, Free convection of copper–water nanofluid in a porous gap between hot rectangular cylinder and cold circular cylinder under the effect of inclined magnetic field, J. Therm. Anal. Calorim. 135 (2) (2019) 1171–1184.
[36] S. Sivasankaran, A. Alsabery, I. Hashim, Internal heat generation effect on transient natural convection in a nanofluid-saturated local thermal non-equilibrium porous inclined cavity, Physica A: Stat. Mech. Appl. 509 (2018) 275–293.
[37] I. Pishkar, B. Ghasemi, A. Raisi, S.M. Aminossadati, Numerical study of unsteady natural convection heat transfer of Newtonian and non-Newtonian fluids in a square enclosure under oscillating heat flux, J. Therm. Anal. Calorim. (2019) 1–14.
[38] A. Jahanbakhshi, A.A. Nadooshan, M. Bayareh, Magnetic field effects on natural convection flow of a non-Newtonian fluid in an L-shaped enclosure, J. Therm. Anal. Calorim. 133 (3) (2018) 1407–1416.
[39] U. Biswal, S. Chakraverty, B.K. Ojha, Natural convection of non-Newtonian nanofluid flow between two vertical parallel plates, Int. J. Numer. Methods Heat Fluid Flow (2019).
[40] R. Mohebbi, A.A. Delouei, A. Jamali, M. Izadi, A.A. Mohamad, Pore-scale simulation of non-Newtonian power-law fluid flow and forced convection in partially porous media: thermal lattice Boltzmann method, Physica A: Stat. Mech. Appl. 525 (2019) 642–656.
[41] B.A. Harab, T. Calisir, S. Baskaya, Numerical investigation of transient natural convection heat transfer of non-Newtonian nanofluids between eccentric annulus, Arab. J. Sci. Eng. 44 (6) (2019) 5631–5646.
[42] A. Alsabery, A. Chamkha, H. Saleh, I. Hashim, Transient natural convective heat transfer in a trapezoidal cavity filled with non-Newtonian nanofluid with sinusoidal boundary conditions on both sidewalls, Powder Technol. 308 (2017) 214–234.
[43] G. Kefayati, Heat transfer and entropy generation of natural convection on non-Newtonian nanofluids in a porous cavity, Powder Technol. 299 (2016) 127–149.
[44] M. Hatami, D. Ganji, Natural convection of sodium alginate (SA) non-Newtonian nanofluid flow between two vertical flat plates by analytical and numerical methods, Case Stud. Therm. Eng. 2 (2014) 14–22.
[45] R. Kumar, M. Kalam, Laminar thermal convection between vertical coaxial isothermal cylinders, Int. J. Heat Mass Transfer 34 (2) (1991) 513–524.
[46] D.A. Nield, A. Bejan, Convection in Porous Media, Springer, 2006.
[47] S.H. Tasnim, R. Hossain, S. Mahmud, A. Dutta, Convection effect on the melting process of nano-PCM inside porous enclosure, Int. J. Heat Mass Transfer 85 (2015) 206–220.
[48] The Finite Element Method for Fluid Dynamics, in: O.C. Zienkiewicz, R.L. Taylor, P. Nithiarasu (Eds.), The Finite Element Method for Fluid Dynamics (Seventh Edition), Butterworth-Heinemann, Oxford, 2014, pp. iii.
[49] J.N. Reddy, An introduction to the finite element method, New York, 1993.
[50] M.H. Matin, W.A. Khan, Laminar natural convection of non-Newtonian power-law fluids between concentric circular cylinders, Int. Commun. Heat Mass Transfer 43 (2013) 112–121.
[51] C. Gau, R. Viskanta, Melting and solidification of a pure metal on a vertical wall, J. Heat Transfer 108 (1) (1986) 174–181.
[52] Q. Sun, I. Pop, Free convection in a triangle cavity filled with a porous medium saturated with nanofluids with flush mounted heater on the wall, Int. J. Therm. Sci. 50 (11) (2011) 2141–2153.
[53] M.A. Sheremet, T. Grosan, I. Pop, Free convection in a square cavity filled with a porous medium saturated by nanofluid using Tiwari and Das' nanofluid model, Transp. Porous Media 106 (3) (2015) 595–610.
[54] A. Brent, V.R. Voller, K. Reid, Enthalpy-porosity technique for modeling convection-diffusion phase change: application to the melting of a pure metal, Numer. Heat Transfer, Part A Appl. 13 (3) (1988) 297–318.
[55] S. Kashani, A. Ranjbar, M. Abdollahzadeh, S. Sebti, Solidification of nano-enhanced phase change material (NEPCM) in a wavy cavity, Heat Mass Transfer 48 (7) (2012) 1155–1166.